

Hexatic-to-Liquid Melting Transition in Two-Dimensional Magnetic-Bubble Lattices

R. Seshadri and R. M. Westervelt

*Department of Physics and Division of Applied Sciences, Harvard University,
Cambridge, Massachusetts 02138*

(Received 17 January 1991)

We report detailed observations of a continuous hexatic-to-liquid melting transition in two-dimensional magnetic-bubble lattices in magnetic garnet films using digital-imaging techniques. Topological defects, diffraction patterns, and translational and orientational correlation functions show that a second-order melting transition occurs via the formation of progressively larger transient defect clusters.

PACS numbers: 64.70.-p, 05.70.Fh, 61.50.Ks, 75.70.Kw

The nature of the melting transition in 2D systems has generated considerable interest and controversy.^{1,2} Building on the ideas of Kosterlitz and Thouless,³ Halperin and Nelson (HN) have suggested that this melting is a second-order two-stage transition driven by the dissociation of dislocation pairs and then disclinations, producing a hexatic phase between the solid and liquid characterized by unpaired dislocations, algebraically decaying orientational order, and exponentially decaying translational order.⁴ Young independently studied the dissociation of dislocation pairs.⁵ Recently, Chudnovsky (C) has suggested that the solid-to-hexatic transition is absent in 2D systems with microscopic disorder, and a hexatic glass rather than a crystalline solid is the most ordered state.⁶ Other theories propose that melting in 2D systems is a first-order transition.⁷ Numerical simulations and experiments on polystyrene colloids,⁸ hard spheres,⁹ liquid crystals, electrons on He, and physisorbed noble gases have probed this transition.¹ A hexatic vortex glass has been seen in disordered high- T_c superconductors.¹⁰

In this Letter, we describe experimental observations of a continuous hexatic-to-liquid melting transition near equilibrium in 2D magnetic-bubble lattices, driven by topological defects in agreement with the HN theory. At higher densities away from the transition we find a C hexatic glass⁶ produced by microscopic disorder. The bubbles can be easily observed and followed in time and space. Polystyrene colloids⁸ share this advantage and display the behavior predicted by HN theory, but with additional vacancies.

These experiments were performed at room temperature on a thin magnetic film of bismuth-substituted iron garnet;¹¹ details of the sample characteristics and experimental setup are given elsewhere.^{12,13} The magnetization is perpendicular to the film and aligned either with or opposed to an applied perpendicular magnetic field H_B . Magnetic bubbles are cylindrical domains of reversed magnetization with radii determined by material parameters and the local field.¹⁴ The bubble radius (3.3 μm) does not change appreciably over the field range used in this experiment,¹⁵ although the bubble density varies by an order of magnitude; the radius is compara-

ble to the film thickness (7.8 μm) and much smaller than the bubble separation (17 to 47 μm). Bubbles interact via a purely repulsive dipolar interaction ($1/r^3$); the dipole moment changes little with H_B and is uniform from bubble to bubble.¹⁵

Polycrystalline bubble lattices with typical crystallite sizes of ~ 12000 bubbles were produced from a sea of bubbles using superimposed ac and dc magnetic fields.¹⁶ All data were taken with a 6.6-Oe-p.p. 40-Hz ac field which causes a slight breathing motion of the bubble radius. Microscopic roughness in the garnet produces a jitter in bubble position which is both spatially and temporally uncorrelated with the jitter of other bubbles, simulating thermal motion.¹⁷ The bubble density ρ was decreased from ~ 4000 to $\sim 500 \text{ mm}^{-2}$ through the melting transition by incrementing H_B from 85 to 95 Oe in small steps. Isolated bubbles collapse at a well defined field, 103 Oe in the absence of an ac field for this film. Each increment in H_B results in the collapse of a few bubbles distributed uniformly over the lattice, creating vacancies that relax into dislocations. After each step the lattice was annealed for 30 min to allow defects to equilibrate.

Bubble lattices were visualized in an optical microscope using polarized light. Grey-scale images of area $1078 \times 808 \mu\text{m}^2$ were recorded using computer video techniques for each step in H_B after annealing. The bubble centers were determined from these images to within ± 1 pixel ($\pm 1.7 \mu\text{m}$). Voronoi constructions¹⁸ were used to isolate topological defects, to determine the lattice constant a , and to obtain the bond information. The maximum number of bubbles in the processed images was ~ 3000 , for which a was ~ 10 pixels (17 μm). Our observations were made on a single crystallite. The grain boundary minimizes external stress and aids in the equilibration of defects. Dislocations of any orientation can reach any point in the lattice by glide from the grain boundary; climb was observed but is not necessary to achieve equilibrium. We measured the diffusion constant for glide by following dislocations across four sequential video frames.

Figure 1 shows sections of images for a typical melting transition. The lattice in Fig. 1(a) has long-range orien-

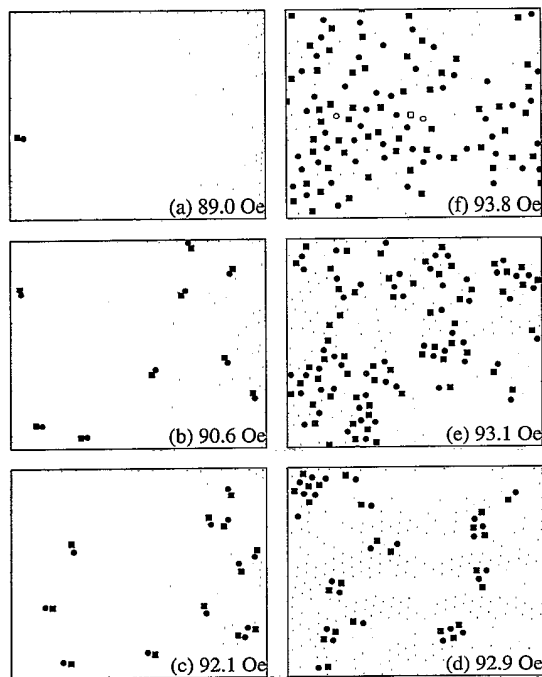


FIG. 1. Melting transition vs field H_B . The dots are bubble centers; the open square, solid squares, solid circles, and open circles are fourfold, fivefold, sevenfold, and eightfold coordinat-ed disclinations in the hexagonal lattice.

tational order, and very low defect concentration and mobility. Here dislocations glide across $\sim 10\%$ of the field of view in the annealing time ($D=0.002a^2/\text{sec}$). In Fig. 1(a) the bubble array is a C hexatic glass⁶ for which translational order is limited by microscopic roughness, not by dislocations (see below). As the bubble density is lowered we observe a HN hexatic⁴ shown in Fig. 1(b), characterized by a gas of dislocations which limits translational order: Here dislocations glide across $\sim 35\%$ of the field of view in the annealing time ($D=0.018a^2/\text{sec}$). Although the lattice is still far from equilibrium, the dislocation gas closely resembles the hexatic described by equilibrium HN theory, because dislocations are created uniformly and can equilibrate locally. The HN hexatic in Fig. 1(c) for lower bubble density has diffusion constants similar to Fig. 1(b). In Fig. 1(c) clustering of dislocations begins to occur, and the clusters evolve continuously in time. Virtual pairs (twisted bonds), vacancies, and interstitials appear as two to four dislocation clusters. In contrast to nuclei in first-order transitions, these transient clusters do not stabilize and grow upon attaining a critical size. In Fig. 1(d) a dramatic increase in the dislocation concentration starts to occur. Isolated dislocations become less common and cluster sizes are larger. Here dislocations glide across $\sim 110\%$ of the field of view in the annealing time ($D=0.069a^2/\text{sec}$). Clusters constantly rearrange and defects go into and out of existence. Time-resolved images show thermal excitation of virtual pairs, and dislo-

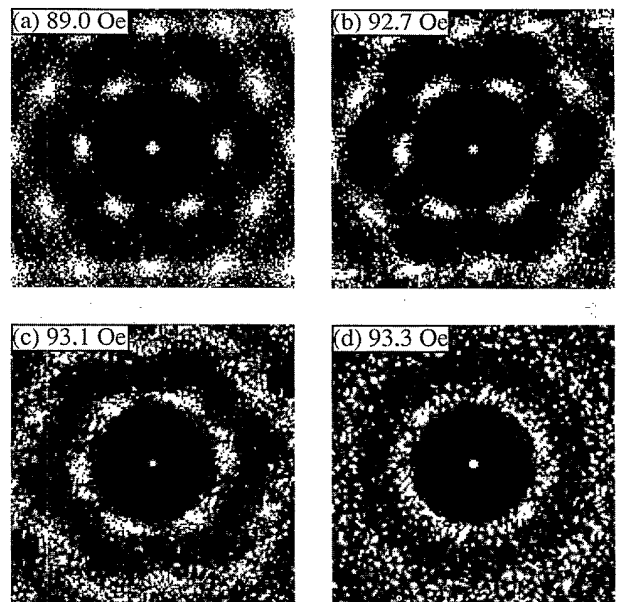


FIG. 2. Two-dimensional structure factor at the magnetic fields H_B indicated (see text).

cation regrouping, creation, and annihilation on time scales ~ 15 sec, indicating that the hexatic is near equilibrium. By criteria given below, the liquid transition occurs near Figs. 1(d) and 1(e). In Fig. 1(e) larger defect clusters form which begin to join each other and percolate across the system: The cluster size is almost equal to the cluster spacing. Finally, in Fig. 1(f) the clusters span the system, dislocations dissociate into disclinations, orientational order diminishes, and the system is a liquid. At these low densities bubbles with four and eight nearest neighbors are often present, as shown in Fig. 1(f). The liquid is characterized by the absence of isolated clusters.

The melting transition is illustrated in a series of 2D structure factors shown in Figs. 2(a)-2(d), computed from the bubble centers using a discrete Fourier transform. The C hexatic glass in Fig. 2(a) shows a sharp sixfold symmetric diffraction pattern [see Fig. 1(a)]. The HN hexatic in Fig. 2(b) has well defined but somewhat smeared peaks. Figure 2(c) displays the diffraction pattern just above the hexatic-to-liquid transition [see Fig. 1(e)]: Here the six first Bragg peaks almost form a ring. In Fig. 2(d) the pattern is that of a liquid.

Figure 3 shows the evolution through the melting transition of the orientational correlation function $G_\Theta(r)$, the two-particle distribution function $g(r)$, and the angular average $S(k)$ of the structure factor, determined from the bubble centers. For the C hexatic glass in Fig. 3, trace a, $G_\Theta(r)$ remains near 1 even for large bubble separations $\sim 40a$. This is the signature for extended orientational order. In traces b-f, $G_\Theta(r)$ decays very slowly with separation r : The orientational order is quasi long range, and corresponds to the HN hexatic shown in Figs.

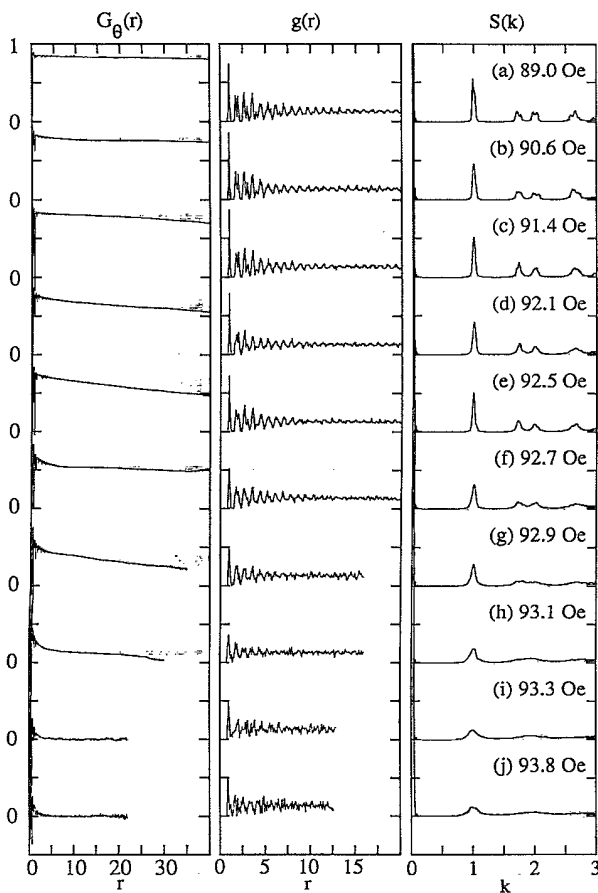


FIG. 3. Orientational correlation functions $G_{\theta}(r)$ vs bond-center separation r in units of the lattice constant a ; normalized two-particle distribution functions $g(r)$ vs bubble separation r in units of a ; and angular averages $S(k)$ of the structure factors vs k in units of the first reciprocal-lattice vector $4\pi/a\sqrt{3}$. The traces a - j correspond to increasing magnetic field H_B , and decreasing bubble density ρ , and show the melting process. For $G_{\theta}(r)$, $g(r)$, and $S(k)$ the dimensionless values 1, 5, and 10 correspond to 1 unit on the vertical axes.

1(b) and 1(c). In traces g and h , $G_{\theta}(r)$ decays more rapidly; these represent the HN hexatic near the melting transition and correspond to Figs. 1(d) and 1(e), respectively. For the liquid in traces i and j , $G_{\theta}(r)$ decays exponentially to zero [see Fig. 1(f)].

The translational correlation function $g(r)$ decreases more rapidly with distance than $G_{\theta}(r)$ at all densities. For the initial lattice shown in trace a , $g(r)$ decays to $1/e$ in $\sim 7a$. This is due in part to the microscopic roughness in the garnet and external stress transmitted from the grain boundary. The short translational correlation lengths, the very-long-range orientational order, and the low defect concentration and mobility imply that this state is a C hexatic glass in analogy with disordered superconductors.^{6,10} For the HN hexatic in traces b - g of Fig. 3 the translational order indicated by $g(r)$ and

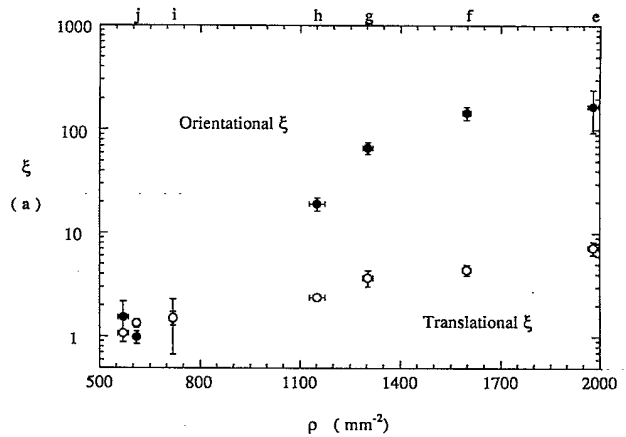


FIG. 4. Translational and orientational correlation lengths ξ in units of lattice spacing a vs bubble density ρ in mm^{-2} for the hexatic-to-liquid transition. The alphabetic labels at the top correspond to those in Fig. 3. Note that the data points correspond to small, even increments in the magnetic field H_B .

$S(k)$ decays more rapidly over $\sim 5a$, with translational order destroyed by unpaired dislocations as predicted in HN theory. For the liquid in traces h - j in Fig. 3 translational order is absent: $g(r)$ decays to zero over $\sim 1a$ to $2a$ and $S(k)$ has broad peaks.

The correlation lengths ξ are shown in Fig. 4. The orientational correlation length was obtained from exponential fits by $G_{\theta}(r)$ over $20a$, and the translational correlation length was determined from least-squares Lorentzian fits to the first Bragg peak in $S(k)$.¹⁹ The sharp drop in orientational order between $\rho = 1600 \text{ mm}^{-2}$ (92.7 Oe) and $\rho = 1100 \text{ mm}^{-2}$ (93.1 Oe) [see Figs. 1(d) and 1(e)] shows the hexatic-to-liquid melting transition. The algebraic exponent η_{θ} was measured from power-law fits by $G_{\theta}(r) \propto r^{-\eta_{\theta}}$. The hexatic-to-liquid transition occurs close to a data point $\rho = 1300 \text{ mm}^{-2}$ [92.9 Oe, Fig. 1(d)] where the measurement $\eta_{\theta} = 0.22 \pm 0.10$ agrees with the equilibrium value $\eta_{\theta} = 0.25$ calculated in HN theory. At low defect concentrations, η_{θ} was measured to be 0.01 (0.03) at 89.0 Oe (90.6 Oe) for the C (HN) hexatic, from which the fraction of area occupied by dislocation cores, c , was calculated using the relation $\eta_{\theta} = 9c/\pi$ from Ref. 9 and found to equal the measured defect concentration of $\sim 0.3\%$ ($\sim 1\%$). The algebraic exponent η_G was extracted from least-squares fits of the form $|k - G|^{-2+\eta_G}$ to the first Bragg peak in $S(k)$. The smallest value measured was $\eta_G = 1.3 \pm 0.1$ over the C-hexatic-glass range $\rho = 3800$ to 3660 mm^{-2} (88.0 to 89.9 Oe). The exponent η_G for the crystalline phase with quasi-long-range translational order cannot exceed 0.33 in HN theory,⁴ confirming that the initial state is not an equilibrium crystal.

To determine the order of the hexatic-to-liquid phase transition, the bubble lattice was placed in a vertical magnetic-field gradient that varied linearly across the

sample. Then H_B was increased slowly until the bubble densities spanning the field of view covered the entire range from the hexatic phase to the liquid phase, and the lattice was allowed to anneal with the applied ac field. Observations showed the absence of a melting front, which confirms the absence of a first-order transition. In addition, the bubble density ρ was always observed to decrease smoothly with increasing H_B . Thus, despite the dramatic increase in dislocation concentration and transient cluster formation, the hexatic-to-liquid transition is continuous. Our results do not agree with the conclusions of numerical simulations on systems with $1/r^3$ potentials, for which first-order transitions have been reported.²⁰

We thank R. Belt and the Airtron Division of Litton Industries for the films, and F. Spaepen, D. S. Fisher, K. L. Babcock, J. Dempsey, J. V. Selinger, and especially D. R. Nelson for helpful conversations, and the condensed-matter theory and robotics groups for computer time. This work was supported by ONR Grants No. N00014-89-J-1592 and No. N00014-89-J-1023.

¹K. J. Strandburg, *Rev. Mod. Phys.* **60**, 161 (1988), and references therein.

²*Ordering in Two Dimensions*, edited by S. K. Sinha (North-Holland, Amsterdam, 1980), and references therein.

³J. M. Kosterlitz and D. J. Thouless, *J. Phys. C* **6**, 1181 (1973).

⁴B. I. Halperin and D. R. Nelson, *Phys. Rev. Lett.* **41**, 121 (1978); D. R. Nelson and B. I. Halperin, *Phys. Rev. B* **19**, 2457 (1979).

⁵A. P. Young, *Phys. Rev. B* **19**, 1855 (1979).

⁶E. M. Chudnovsky, *Phys. Rev. B* **40**, 11 355 (1989).

⁷D. S. Fisher, B. I. Halperin, and R. Morf, *Phys. Rev. B* **20**, 4692 (1979); T. V. Ramakrishnan, *Phys. Rev. Lett.* **48**, 541 (1982); S. T. Chui, *Phys. Rev. Lett.* **48**, 933 (1982); *Phys. Rev. B* **28**, 178 (1983); H. Kleinert, *Phys. Lett.* **95A**, 381 (1983); B. Joos and M. S. Duesbery, *Phys. Rev. Lett.* **55**, 1997 (1985); *Phys. Rev. B* **33**, 8632 (1986).

⁸C. A. Murray and D. H. Van Winkle, *Phys. Rev. Lett.* **58**,

1200 (1987); C. A. Murray, W. O. Sprenger, and R. A. Wenk, *Phys. Rev. B* **42**, 688 (1990).

⁹D. R. Nelson, M. Rubinstein, and F. Spaepen, *Philos. Mag. A* **46**, 105 (1982).

¹⁰C. A. Murray, P. L. Gammel, D. J. Bishop, D. B. Mitzi, and A. Kapitulnik, *Phys. Rev. Lett.* **65**, 2312 (1990).

¹¹R. F. Belt and J. B. Ings, *SPIE J.* **753**, 142 (1987).

¹²K. L. Babcock and R. M. Westervelt, *Phys. Rev. A* **40**, 2022 (1989).

¹³R. Seshadri and R. M. Westervelt (to be published).

¹⁴A. H. Eschenfelder, *Magnetic Bubble Technology* (Springer-Verlag, New York, 1981); A. P. Malozemoff and J. C. Slonczweski, *Magnetic Domain Walls in Bubble Materials* (Academic, New York, 1979).

¹⁵The bubble radii vary little with coordination. The distribution of bubble radii at a given field is sharp with standard deviation $< 0.4 \mu\text{m}$. The mean radius $3.26 \mu\text{m}$ changes by $< 0.13 \mu\text{m}$ over the entire field range.

¹⁶G. R. Woolhouse and P. Chaudhari, *Philos. Mag.* **31**, 161 (1974).

¹⁷We do not observe any convective or coherent bubble motion in the ac field. For $\rho < 50 \text{ mm}^{-2}$ we determine an effective temperature $T \sim 10^5 \text{ K}$ from $k_B T = D/B$, where D and B are the measured diffusion constant and mobility. The diffusion constant is fitted by $D = b^2 \nu \exp(-\phi/T)$ with $b = 0.6 \mu\text{m}$ and $\phi = 10^6 \text{ K}$. The dimensionless parameter $\Gamma_c = (\mu^2/a_c^3)/k_B T$ is ~ 30 , where μ is the bubble dipole moment and a_c is a at the transition. At the transition the rms bubble displacement is $0.12a$, and the standard deviation of the distribution of lattice spacings is $0.10a$.

¹⁸F. P. Preparata and M. I. Shamos, *Computational Geometry, an Introduction* (Springer-Verlag, New York, 1985).

¹⁹The instrumental limit to ξ is determined by the width of the apodizing window which was selected to be twice the largest measured ξ . The fundamental limit is determined by the image width, which is $\sim 50a$ for the most ordered lattice. The results shown are averaged over several images spanning a large area. The ac field was slowly reduced to zero before recording each image, and the error due to image digitization is negligible.

²⁰R. K. Kalia and P. Vashishta, *J. Phys. C* **14**, L643 (1981); V. M. Bedanov, G. V. Gadiyak, and Yu. E. Lozovik, *Phys. Lett.* **92A**, 400 (1982).